Kobe University Repository : Kernel

PDF issue: 2026-11-06

Enhanced acceleration transmission via dual-beam frequency conversion interposer for design-flexible MEMS vibration energy harvesters

Ueno, Hidetaka
Ichige, Ryo
Morishita, Kota
Toshiyoshi, Hiroshi
Suzuki, Takaaki

(Citation)
Sensors and Actuators A: Physical,408:118002

(Issue Date)
2026-10-01

(Resource Type)
journal article

(Version)
Version of Record

(Rights)
© 2026 The Author(s). Published by Elsevier B.V.
This is an open access article under the Creative Commons Attribution 4.0 International license

(URL)
https://hdl.handle.net/20.500.14094/0100504313

Sensors & Actuators: A. Physical 408 (2026) 118002

Contents lists available at ScienceDirect

Sensors and Actuators: A. Physical

journal homepage: www.journals.elsevier.com/sensors-and-actuators-a-physical

Enhanced acceleration transmission via dual-beam frequency conversion interposer for design-flexible MEMS vibration energy harvesters

Hidetaka Ueno [a,*], Ryo Ichige [b], Kota Morishita [b], Hiroshi Toshiyoshi [c], Takaaki Suzuki [b,**]

[a] Center for Advanced Medical Engineering Research & Development (CAMED), Kobe University, 1-5-1 Minatojima-minamimachi, Chuo-ku, Kobe, Hyogo 650-0047, Japan
[b] Division of Electronics and Mechanical Engineering, Gunma University, Kiryu, Gunma 376-8515, Japan
[c] Institute of Industrial Science (IIS), The University of Tokyo, 4-6-1 Komaba, Meguro-ku, Tokyo 153-8505, Japan

ARTICLE INFO

Keywords:
Vibration energy harvester
Bistable
Frequency conversion
Interposer
Micro
Electro Mechanical Systems

ABSTRACT

An interposer with a bistable structure and no internal stress can convert random environmental vibrations and efficiently transmit vibrational energy to micro-electromechanical systems vibrational energy harvesters (MEMS VEHs). However, with conventional methods, the MEMS VEH must be designed to match the interposer, significantly limiting its design flexibility. This study presents an extended approach for broadening the recovery vibration bandwidth and efficiently transmitting acceleration to a MEMS VEH using a dual-beam frequency conversion interposer (dual-beam-FCI). The MEMS VEH receives large acceleration induced by a snap-through (ST) of a bistable beam. A comparison between the theoretically calculated energy required for ST and the energy input during the vibration experiments revealed that ST occurred with less energy than that theoretically calculated, regardless of the input frequency, i.e., even at low input frequencies of approximately 10–20 Hz. Therefore, the dual-beam-FCI, which can be integrated into various MEMS VEHs, is useful for broadening the recovery bandwidth and efficiently harvesting low-frequency vibrational energy, particularly in the range of 10–20 Hz. The dual-beam-FCI can generate large accelerations via ST without imposing design limitations on the integrated MEMS VEH and thus shows applications for environmental energy harvesting using various MEMS VEHs.

1. Introduction

Wireless sensors, which serve as independent sensor nodes and collect various data from the Internet of Things (IoT), require compact onboard batteries. However, conventional batteries are generally unsuitable as power sources for sensor nodes that require long-term autonomous operation. This is primarily because of their limited electrical storage capacity and the high cost associated with battery replacement [1–3].

Among the various types of energy harvesters (EHs) that convert ambient energy directly into electrical energy, micro-electromechanical system vibration energy harvesters (MEMS VEHs) have attracted attention as potential power sources for autonomous sensor nodes. VEHs offer notable advantages in terms of efficiency and versatility owing to the relatively high energy density of vibrations and their reduced sensitivity to environmental fluctuations. Furthermore, MEMS VEHs, which are fabricated using microfabrication techniques commonly used in semiconductor processing, can be easily miniaturized. This renders them highly promising compact power sources for small sensor nodes requiring autonomous operation under diverse environmental conditions [4–6].

MEMS VEHs typically generate electrical power via the oscillation of an oscillatory structure in response to ambient vibrations [7]. In vibration-based energy harvesting, energy conversion efficiency can be enhanced by matching the resonance frequency with the frequency of ambient vibrations that induce resonance. Generally, the natural frequency of a resonator is inversely correlated with its size. Consequently, MEMS VEHs with volumes ranging from a few cubic centimeters to a few cubic millimeters tend to resonate at high frequencies, typically exceeding several hundred hertz [8]. However, many ambient

* Corresponding author.
** Correspondence to: 1-5-1 Tenjin-cho, Kiryu, Gunma 376-0052, Japan.
E-mail addresses: hueno@people.kobe-u.ac.jp (H. Ueno), suzuki.taka@gunma-u.ac.jp (T. Suzuki).

https://doi.org/10.1016/j.sna.2026.118002
Received 12 March 2026; Received in revised form 8 May 2026; Accepted 13 May 2026
Available online 15 May 2026
0924-4247/© 2026 The Author(s). Published by Elsevier B.V. This is an open access article under the CC BY license (http://creativecommons.org/licenses/by/4.0/).

vibrations observed in real-world environments fall within the low-frequency range, which is generally below 100 Hz [9–12]. Therefore, MEMS VEHs cannot easily harvest vibrational energy efficiently. To address this issue, various MEMS VEHs have been designed for low-frequency operations [13–18]. However, further enhancement in practical applications, such as size, integration, and production cost, is necessary. Moreover, because the amplitude and frequency of environmental vibrations fluctuate randomly over time, conventional MEMS VEHs struggle to stably and continuously convert vibrational energy into electrical energy.

To enhance the power generation efficiency of MEMS VEHs, studies have proposed a novel approach that integrates a bistable structure exhibiting nonlinear vibrations into the interposer, which is a component that electrically and mechanically connects circuit boards to devices such as MEMS VEHs [19–21]. Bistable structures are expected to improve energy-conversion efficiency by transforming random vibrations, including low-frequency vibrations in a general environment, into a frequency that is close to the resonance frequency of the MEMS VEHs. A bistable structure is characterized by the presence of two stable equilibrium positions. Its vibrational behavior can be broadly classified into two modes: intrawell oscillations, where motion remains confined within a single potential well, and interwell oscillations, which involve transitions between two potential wells and are also known as snap-through (ST) [22–23]. Although chaotic vibrations are also present, they occur only under highly specialized conditions and are therefore not discussed in detail in this study. Interwell oscillations include impulse vibrations due to ST. Because ST is driven by releasing the potential energy inherent in the bistable structure, the resulting acceleration is substantially independent of the amplitude and frequency of the input vibration [24–26]. Therefore, by incorporating a bistable structure into the interposer, a wide range of ambient vibrations can be efficiently transformed and supplied to the MEMS VEH, thereby enhancing its ability to efficiently harvest vibrational energy under various environmental conditions [27].

Bistable structures are typically assembled using combinations of small magnets or structures with internal stresses [28–32]. However, interposer structures that incorporate magnets or internally stressed components are not suitable for batch fabrication, assembly, and packaging processes based on semiconductor/MEMS manufacturing technologies. This poses challenges in terms of miniaturization and mass production, which are requirements for power sources in sensor nodes. To address this issue, a vibrational energy conversion approach that employs non-internal stress curved beams as bistable structures has been proposed [33–36]. Because these beams can be fabricated using conventional semiconductor manufacturing processes, they can be easily batch-manufactured and assembled using MEMS VEHs [37–39]. Furthermore, in our previous study, using a structure without internal stress, we observed that the oscillatory waveform of a MEMS VEH can induce ST in a bistable structure, thereby efficiently supplying vibrational energy to the MEMS VEH [40]. However, this approach, which relies on the oscillatory structure of the MEMS VEH to induce ST, significantly restricts its design flexibility.

In this study, we presented an extended approach using a dual-beam frequency conversion interposer (dual-beam-FCI) that converts ambient vibrational energy through a bistable structure and efficiently transmits it to a MEMS VEH without constraining the design flexibility of the MEMS VEH. In this method, MEMS VEHs based on various principles, such as piezoelectric, electromagnetic, and electrostatic mechanisms, can be simply integrated into the dual-beam FCI, enabling efficient energy harvesting from diverse vibration environments. To simulate the function of the dual-beam FCI, we fabricated a dual-beam monolithic structure (DBMS) comprising bistable and non-bistable beams, both free from internal stress, with structures similar to those in the dual-beam-FCI. By comparing the input and output accelerations through the DBMS, we evaluated the acceleration transmission efficiency of the dual-beam-FCI. Table 1 presents spell-out forms of abbreviations.

Table 1
Spell-out forms of abbreviations.

Abbreviation	Definition
VEH	Vibration energy harvester
MEMS	Micro-electromechanical systems
Dual-beam-FCI	Dual-beam frequency conversion interposer
DBMS	Dual-beam monolithic structure as a model for Dual-beam-FCI
ST	Snap-through
F-D curve	Force-displacement curve
FEM	Finite element method

2. Concept of this study

The vibrational behavior of the dual-beam-FCI was verified using the DBMS. Fig. 1 shows conceptual images of the DBMS, which is a model of the dual-beam-FCI. Although the power generation mechanism of MEMS VEHs differs depending on the device, all MEMS VEHs have connection points for transmitting the generated electrical energy and connecting it mechanically. The dual-beam-FCI has two types of beams that convert vibrations and an electrode that receives electrical energy from the MEMS VEH and transmits it to an external circuit, such as an IC. The MEMS VEH and dual-beam-FCI are connected via a connection point. Input vibration, including impulse vibration (purple arrow in Fig. 1(A)), induces nonlinear vibration using the ST of the first beam of the dual-beam-FCI and linear vibration of the second beam. Input vibration from the environment and output vibration converted by the two beams are input to the MEMS VEH (red arrow in Fig. 1(A)). The ST of the first beam induces considerable displacements and accelerations, the magnitudes of which, in principle, are not correlated with the frequency of the input vibration. Therefore, the first beam can transmit environmentally induced vibration energy, which is a broadband random vibration, to the second beam regardless of its frequency. In addition, the vibration of the second beam induces ST of the first beam [40]. In other words, input vibration from the environment and the vibrations of the first and second beams exhibit a complex relationship, thus producing output vibration.

Because the composite vibration induced by the complex interaction between the first and second beams was input into the MEMS VEH, a verification model with a structure mimicking the dual-beam-FCI was developed to clarify the magnitude and frequency of the acceleration input to the MEMS VEH. The verification model DBMS used in this study has a first and second beam corresponding to the bistable first beam and non-bistable second beam of the dual-beam-FCI, respectively (Fig. 1(B)). The curved first beam was designed to buckle and function as a bistable structure. An acceleration sensor was integrated at the location of the MEMS VEH. We evaluated the acceleration of the frequency-converted vibration input from the dual-beam-FCI to the MEMS VEH and the acceleration transmission efficiency of the dual-beam-FCI using an acceleration sensor. To this end, the sensor measured the magnitude and frequency of the vibration acceleration on the second beam of the DBMS when an external vibration was applied to the DBMS.

3. Materials and methods

3.1. Modal analysis

The natural frequencies of the two beams in the DBMS were measured via modal analysis using a finite element method (FEM), which was performed using computer-aided engineering software (COMSOL, Inc.; COMSOL Multiphysics 5.4). The FEM analysis model is shown in Fig. 2. The DBMS had two oscillatory beams; the first being curved and the second straight. The first beam had a thin film hinge part; the thickness and length of which are 0.1 mm and I, respectively. The initial displacement of the first beam was H. The value of I was set in increments of 4 mm, ranging from 0 to 12 mm, and the value of H was set in increments of 2 mm, ranging from 0 to 6 mm. Each model is

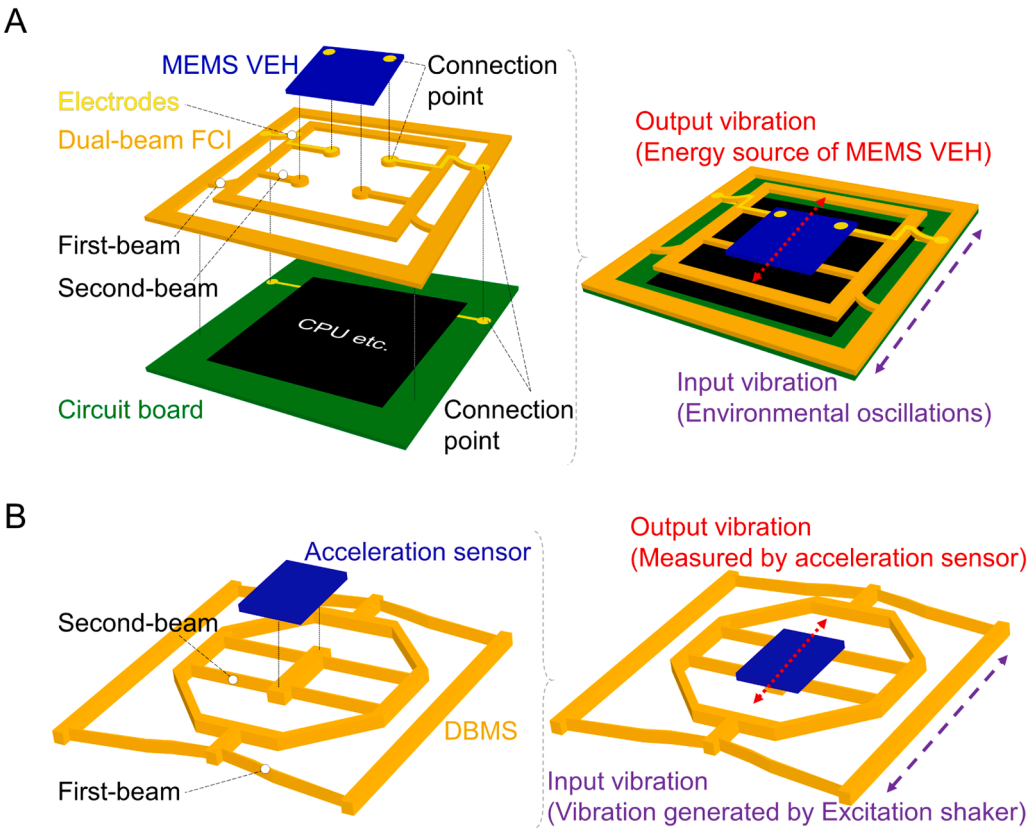
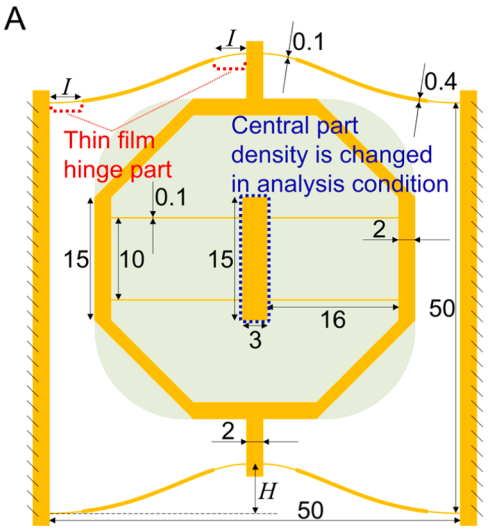


Fig. 1. Conceptual image of dual-beam monolithic structure (DBMS) for simulating the dual-beam-FCI assembled to micro-electromechanical systems vibrational energy harvesters (MEMS VEHs). (A) Schematic of energy harvesting system composed of dual-beam-FCI and MEMS VEH. (B) Schematic of DBMS, which is a model of the dual-beam-FCI assembled to the acceleration sensor.



B

Design and analysis conditions	
I [mm]:	0, 4, 8, 12
H [mm]:	0, 2, 4, 6
Thickness [mm]:	5
Material:	Polycarbonate
Density [kg/m^3]:	1200, (40000)
Young's modulus [GPa]:	2.25
Poisson's ratio [-]:	0.35

Fig. 2. Analytical model of dual-beam-FCI. (A) Overall analytical model of DBMS. The unit in the figure is a millimeter. (B) Analysis conditions.

expressed using the values of *I* and *H*. For example, the model with a 4-mm thin-film hinge part and 2-mm initial displacement is expressed as I4H2. In the FEM analysis, the change in the vibration mode due to the mass of the central part mimicking the MEMS VEH was evaluated by changing the density of the central part of the second beam of the DBMS. The densities of the central part were 1200 and 40,000 kg/m^3. The analysis results, natural frequency, and mode order for each model were plotted using MathWorks Inc. (MATLAB 6.1). Furthermore, an analysis was performed when the vibration of the second beam was suppressed by setting the part covered by the green frame in Fig. 2(A) as a rigid body, and the influence of the second-beam vibration on the vibration mode of the DBMS was evaluated.

3.2. Fabrication

Among the models analyzed, four types of DBMS were manufactured by unidirectional processing of polycarbonate plates. The DBMS was fabricated by cutting a 5-mm-thick polycarbonate plate (PC 1600,

TAKIRON Corporation) in one direction using an NC milling machine (MDX-40A, Roland DG Corporation) and an end mill of diameter 2 mm. By 5 mm thickness of PC, the DBMS bending caused by gravity is prohibited. This processing method enabled the fabrication of a DBMS with curved beams without internal stress. The structure for installation on the vibrator is the same as that used in the literature [40].

3.3. Vibration experimental setup

The vibration characteristics of the fabricated DBMS were evaluated through a vibration experiment using an acceleration sensor. The vibration experimental system and the specifications of the sensor (LIS3DH, STMicroelectronics, mass: 1.5 g) are shown in Fig. 3. The DBMS with the acceleration sensor was fixed on an excitation shaker. The vibration direction of the DBMS beam was perpendicular to the direction of gravity; therefore, gravitational acceleration did not affect the vibration of the DBMS beams. The acceleration sensor was fixed at the center of the second beam of the DBMS. A 9.0-g weight was also attached to the center of the second beam using double-sided tape. This reproduced almost the same conditions as those of the analysis model, in which the density of the central part was 40,000 kg/m^3. An accelerometer was attached to the excitation shaker, enabling the shaker to reproduce the set maximum vibration acceleration amplitude through feedback control.

The maximum acceleration amplitude set by the excitation shaker software and the acceleration acquired by the acceleration sensor fixed to the DBMS were different. In this experiment, the acceleration acquired from the accelerometer was used as the input acceleration.

3.4. Evaluation of vibrational waveforms and frequency conversion

To determine a conversion function for the input vibration of the DBMS, the acceleration of the output vibration was measured using an acceleration sensor fixed to the second beam of the DBMS. The acceleration was measured when a 10-Hz vibration, which is a relatively low frequency among the vibrations in the general environment, was input to the I4H4 model. Previous studies have shown that the vibration energy recovery efficiency of a MEMS VEH with a bistable structure can be improved by a sudden increase in acceleration caused by an ST [40]. Therefore, the vibration frequency and acceleration of the second beam in the intra-and interwell oscillations near the ST of the DBMS were measured. In addition, the acceleration was calculated using a fast Fourier transform (FFT) to determine the main frequency.

3.5. Verification of acceleration transmission and amplification effect

To explain the effect of differences in the shape of the DBMS on the output acceleration, the I4H2, I4H4, and I8H2 models were used and the acceleration generated on the second beam was measured when the input vibration frequency was fixed at 10 Hz and the input acceleration varied from 0.1 to over 2.0 G. The accelerations measured by the accelerometer and acceleration sensor on the second beam of the DBMS were compared. The root mean squares of both accelerations were compared to evaluate the acceleration conversion function of the DBMS.

3.6. Dependency analysis of ST thresholds and theoretical comparison

To elucidate the relationship between the input vibration frequency and the ST of the DBMS, the acceleration at which the DBMS induces the ST was measured while varying the frequency of the input vibration. For I4H2, I4H4, I8H2, and I8H4, the frequency of the input acceleration was changed from 10 to 40 Hz, and the input acceleration at which the ST occurred was measured. In addition, to clarify the effect of differences in mass on the second beam, the experiment was performed by attaching a 9.0 or 18.0-g weight to the second beam of the DBMS. The magnitude and frequency of the input acceleration to the DBMS were measured, and the effects of the differences in the shape of the DBMS and the mass placed on the second beam on the ST were clarified.

To induce ST, input vibration energy is required to overcome the potential barrier between stable equilibrium points. The efficiency of the vibration power generation of the DBMS was evaluated by comparing the ST generation acceleration calculated via the FEM analysis with the ST generation acceleration of the DBMS obtained by the vibration experiment. The analysis targeted four models, namely I4H2, I4H4, I8H2, and I8H4. The potential energy required to induce ST was calculated using the integral of the F–D curve. The input energy is the kinetic energy generated when the input vibration acts on the weight of the straight beam. As the input acceleration from the vibrator is a sine wave, the acceleration $a(t)$ can be expressed as

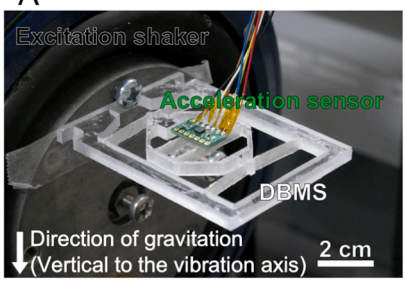
$$a(t) = A\sin\frac{2\pi}{T}t \tag{1}$$

Here, A is the acceleration amplitude, and T is the period. The displacement $x(t)$ is obtained by integrating $a(t)$ twice with respect to time assuming zero initial displacement and velocity, and is expressed as:

$$x(t) = -A\frac{T^2}{4\pi^2}\sin\frac{2\pi}{T}t \tag{2}$$

Because this is a periodic function and the direction of the applied force reverses in half a cycle, the displacement–acceleration curve expressed by Eqs. (1) and (2) is integrated over an integration interval of T/2, and the input energy per unit acceleration is calculated by multiplying it by the mass of the central part. The ST generation acceleration is calculated by dividing the potential barrier by the input energy. The ST generation efficiency of the DBMS is determined by comparing the calculated ST generation acceleration with the ST generation acceleration obtained from a vibrational experiment.

A



B

Acceleration sensor conditions	
Measurement range [G]:	± 2, ± 4, ± 8, ± 16
Sensitivity [mg/digit]:	1, 2, 4, 12
Resolution [bits]:	8, 10, 12
Output data rage [Hz]:	5000
Bandwidth [Hz]:	2500

Fig. 3. Vibrational experimental system and condition. (A) Photograph of experimental system. The vibration axis is vertical to the direction of gravity. (B) Acceleration sensor conditions.

4. Results and discussion

4.1. Modal analysis

The FEM analysis was conducted using the analytical models of 16 dual-beam-FCIs with different *I* and *H*. The deformation shapes obtained from the modal analysis under the resonance of the first and second beams are shown in Fig. 4. When the first beam is in resonance, it exhibits significant deformation, and the second beam exhibits considerable deformation. Although the second beam deforms during the resonance of the first beam, the central part where the acceleration sensor is integrated exhibits negligible vibration (Fig. 4(A)). By contrast, during the resonance of the second beam, the central part of the second beam, where the acceleration sensor is integrated, exhibits significant deformation, whereas the first beam does not undergo significant deformation (Fig. 4(B)). The modal analysis results show that the vibrational deformation shapes of the dual-beam-FCI can be used to identify the natural frequency that corresponds to each mode and beam structure.

The modal analysis helps to determine the natural frequencies up to the sixth mode. The natural frequencies and eigenmode numbers of each model are shown in Fig. 5. The horizontal axis of the graph represents the design parameter *I* or *H* for each model, and the vertical axis represents the resonance frequency of each eigenmode number. The color of each plot corresponds to the eigenmode number. Regardless of the first-beam geometry, the natural frequency of the second beam decreases as the density at the center of the second beam increases (Fig. 5(A) and (B)). Because a negative correlation exists between mass and natural frequency, it was inferred that the models with a lower density at the central part of the second beam exhibited higher natural frequencies. However, when the second beam was actively vibrating, the mode number of the first beam associated with the generation of the ST varied depending on the central density of the second beam, although the natural frequency remained almost unchanged (Fig. 5(C) and (E)). Conversely, when the second beam did not vibrate, the natural frequency of the first beam changed significantly (Fig. 5(D) and (F)). These results show that in a two-degree-of-freedom vibrational system, where the second beam is oscillating, the first beam responsible for generating the ST is minimally affected by the presence of the integrated MEMS VEH on the second beam. Therefore, in the proposed dual-beam-FCI with two degrees of freedom, the first beam exhibits a considerable displacement and high output acceleration accompanied by ST, without being significantly affected by the mass of the MEMS VEH integrated on the second beam. This confirms that the proposed dual-beam-FCI does not significantly affect the design of the MEMS VEH. The resonance frequencies of each beam and the acceleration levels at which ST occurs have been reported in a previous study [40]. In addition, it has been shown that ST can occur at lower acceleration levels in models with lower stiffness and smaller initial displacement. Furthermore, the transition process from intrawell oscillations to ST was experimentally confirmed to be consistent with the analytical model. These results indicate qualitative agreement between the analytical model and the fabricated DBMS.

4.2. Evaluation of vibrational waveforms and frequency conversion

The acceleration output generated by the second beam of the DBMS during intrawell and interwell oscillations was measured using the I4H4 model. The frequency of the input vibration was fixed at 10 Hz, and the input acceleration was varied. The resulting oscillatory waveforms of the output acceleration acquired using the acceleration sensor and their corresponding FFT analyses are shown in Fig. 6. In Fig. 6(A), (B), and (C), the horizontal axis represents the measurement time and the vertical axis represents the acceleration measured by the acceleration sensor. In the FFT results shown in Fig. 6(D), (E), and (F), the horizontal axis represents the frequency of the output acceleration obtained from the acceleration sensor, and the vertical axis represents the amplitude.

The time history response of the vibration and its FFT result when the input acceleration is set to 2.0 G are shown in Fig. 6(A) and (D). Based on visual observation, the vibration under this condition was identified as intrawell oscillations without the occurrence of ST. Although the acceleration waveform exhibited an approximately constant period and amplitude, the oscillation was asymmetric. This asymmetry is attributed to the first beam of the DBMS. Because the first beam is pre-curved to function as a bistable structure, it induces asymmetric vibration when the second beam undergoes oscillation. The FFT analysis reveals that the dominant frequency is an input frequency of 10 Hz, as indicated by the blue hatch in Fig. 6(D). In addition, a frequency peak is observed in the range of 20–30 Hz, as indicated by the red hatch in Fig. 6(D). For intrawell oscillations without an ST, the peak observed between 20 and 30 Hz is considered to be caused by the vibration of the second beam because its stiffness is lower than that of the first beam.

The vibration time history response and FFT processing results when the input acceleration is 2.7 G are shown in Fig. 6(B) and (E). Visual

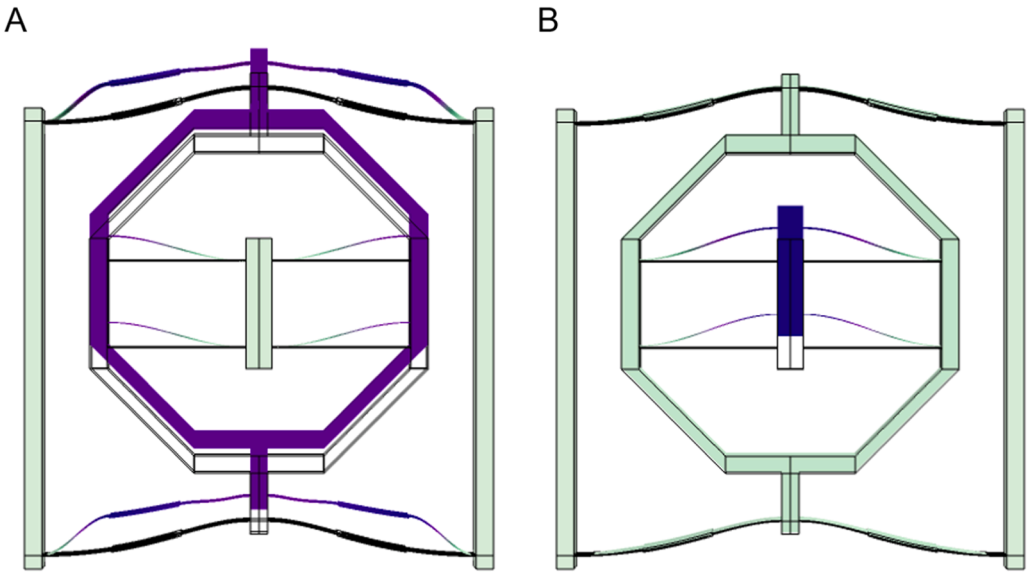


Fig. 4. Resonance vibration shape of dual-beam-FCI in modal analysis. (A) Resonance vibration shape of first-beam. (B) Resonance vibration shape of second-beam.

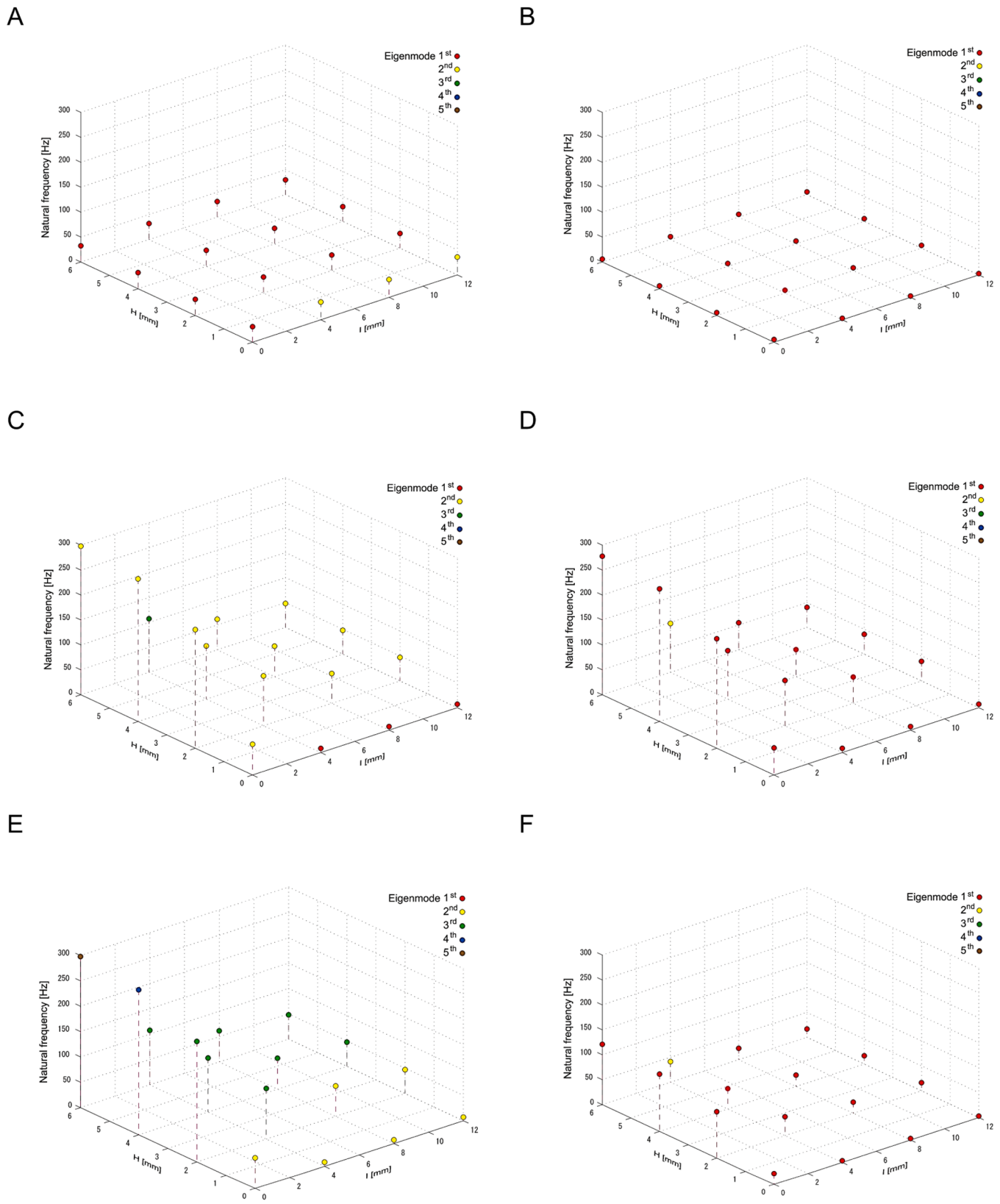


Fig. 5. Natural frequency of each beam of dual-beam-FCI in modal analysis. The colors of plots represent the eigenmodes. (A) The natural frequency of the second-beam of dual-beam-FCI in modal analysis. The density of the central part is 1200 kg/m^3. (B) The natural frequency of the second-beam of dual-beam-FCI in modal analysis. The density of the central part is 40,000 kg/m^3. (C) The natural frequency of the first-beam of dual-beam-FCI in modal analysis. The density of the central part is 1200 kg/m^3. The second-beam is vibrated. (D) The natural frequency of the first-beam of dual-beam-FCI in modal analysis. The density of the central part is 1200 kg/m^3. The second-beam is not vibrated. (E) The natural frequency of the first-beam of dual-beam-FCI in modal analysis. The density of the central part is 40,000 kg/m^3. The second-beam is vibrated. (F) The natural frequency of the first-beam of dual-beam-FCI in modal analysis. The density of the central part is 40,000 kg/m^3. The second-beam is not vibrated. Detailed values of the natural frequencies are given in the Supplementary Material.

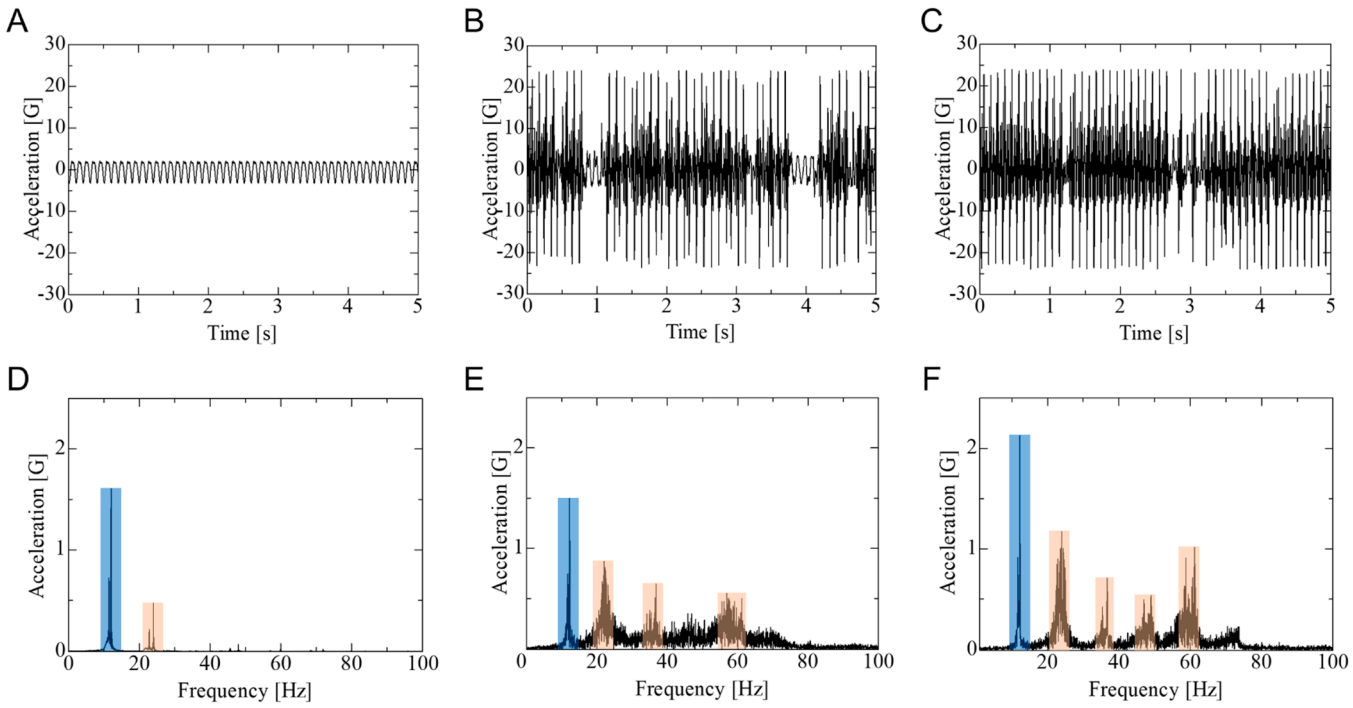


Fig. 6. Time history and fast Fourier transform (FFT) spectrum of acceleration of the I4H4. (A) Time history with 2.0 G input acceleration. (B) Time history with 2.7 G input acceleration. (C) Time history with 3.0 G input acceleration. (D) FFT spectrum with 2.0 G input acceleration. (E) FFT spectrum with 2.7 G input acceleration. (F) FFT spectrum with 3.0 G input acceleration. Blue hatch indicates vibration frequency that is close to input vibration from the excitation shaker. Red hatch indicates the peak frequency of converted vibration by DBMS.

observation shows that this vibration condition induces ST, which is an interwell oscillation in which the acceleration sensor moves between stable equilibrium points. The time history response exhibits a nonlinear waveform with a constant period and magnitude. FFT processing shows that the largest frequency component of the vibration is 10 Hz, which is the same as the input frequency (blue hatch in Fig. 6(E)). Peaks were observed between 20 and 30 Hz, 30 and 40 Hz, and 50 and 60 Hz (red hatch in Fig. 6(E)). This indicates that these multiple peaks are caused by the nonlinear vibration of the ST of the first beam.

The vibration time history response and FFT processing results when the input acceleration is 3.0 G are shown in Fig. 6(C) and (F). Visual observations show that this vibration condition induces ST, and the acceleration sensor undergoes interwell oscillations, transitioning between stable equilibrium positions. The time history of the acceleration displays a nonlinear waveform. The FFT analysis shows that the dominant frequency is 10 Hz, which corresponds to the input frequency (blue hatching in Fig. 6(F)). Additional peaks were observed in the frequency ranges of 20–30, 30–40, 40–50, and 55–65 Hz (red hatch in Fig. 6(F)). Compared with the response under 2.7 G input acceleration, the number of frequency peaks increased, and the relative magnitudes of these peaks also changed. For example, although the third-largest acceleration peak under 2.7 G was observed in the range of 30–40 Hz, under 3.0 G, it shifted to the range of 55–65 Hz. These results indicate that interwell oscillations involving ST produce multiple frequency peaks whose magnitudes and orders vary with the amplitude of the input vibration. This variation is attributed to the reduced frequency correlation between the input excitation and ST-induced vibration due to the nonlinear dynamic behavior of the first beam.

This vibrational experiment shows that the frequency and peak magnitude of the vibration generated by the second beam can be determined by the magnitude of the input vibration, for both intrawell and interwell oscillations generated by ST. Therefore, by designing a dual-beam-FCI considering the magnitude of vibration in the environment and the resonance of the MEMS VEH, the vibration energy of the peak magnitude can be applied to the MEMS VEH integrated on the second beam, enabling efficient energy conversion from the vibration.

4.3. *Verification of acceleration transmission and amplification effect*

The output acceleration generated by the DBMS under different input accelerations was measured using an acceleration sensor integrated into the second beam of the DBMS. Fig. 7 shows the root mean square (RMS) values of the output acceleration measured on the second beam for the I4H2, I4H4, and I8H2 models at a constant excitation frequency of 10 Hz with varying input accelerations. The horizontal axis represents the RMS of the input acceleration measured by an accelerometer directly integrated into the stage of the excitation shaker, and the

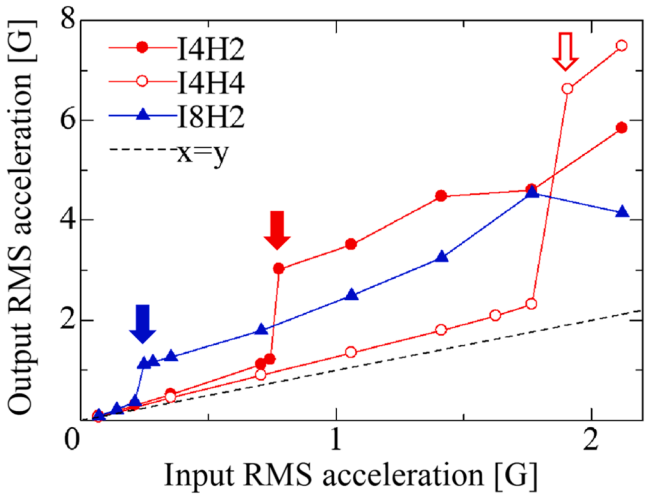


Fig. 7. Root mean square (RMS) accelerations of input and output vibrations in each DBMS model. Arrows indicate the minimum input RMS acceleration that caused ST.

vertical axis represents the RMS values of the output acceleration generated on the second beam of each DBMS in response to the corresponding input acceleration.

At a low input acceleration, all DBMSs exhibited intrawell vibration, and the output acceleration was approximately equal to the input. For all models, a sharp increase in output acceleration was observed near the ST. The output acceleration was consistently greater than the input acceleration across all cases. Among the three models, I8H2 required the lowest input acceleration to induce ST, and I4H4 required the highest. Immediately after ST, I8H2 exhibited the smallest output acceleration, and I4H4 exhibited the largest. This behavior could be attributed to the combined effects of the interaction between the two beams. Specifically, the coupled motion of the first and second beams led to an effective amplification of the acceleration response at the sensor location. In addition, since the acceleration sensor was mounted on the second beam, the measured signal inherently included contributions from both beams, resulting in a larger apparent output compared to the input.

Our previous study demonstrated that models with lower energy barriers between stable equilibrium positions undergo ST at lower energy levels. Moreover, we observed that the magnitude of output acceleration following ST correlated with the energy required for transitioning between stable equilibrium positions [40]. The results of this study support these findings. However, although a previous study has reported output acceleration exceeding the input only immediately after ST, the current measurements from acceleration sensors integrated on the second beam consistently show output accelerations greater than the input. This discrepancy can be attributed to the measurement location. The previous study measured the acceleration from only the first beam, whereas the present study measured the combined acceleration resulting from the vibrations of both the first and second beams. Consequently, the measured output accelerations in this study exceeded those reported in previous studies. Therefore, integrating the MEMS VEH onto the second beam, which induces the ST of the first beam, enables the MEMS VEH to be subjected to significantly amplified accelerations.

4.4. Dependency analysis of ST thresholds and theoretical comparison

The magnitude of the input acceleration at which ST occurred was evaluated by varying the frequency of the input vibration. Four models (I4H2, I4H4, I8H2, and I8H4) were evaluated. The masses integrated at the center of the second-beam had values 9.0 and 18.0 g. The magnitude of the input acceleration that induced ST for each model under these two masses is shown in Figs. 8(A) and 8(B), respectively. In the graphs, the horizontal axis represents the frequency of the input vibration, and the vertical axis indicates the input acceleration at which ST occurred.

The input acceleration at which ST occurred increased quadratically across all models. In the low-frequency domain, ST occurred at lower input accelerations. Particularly in the frequency range below 20 Hz, all models except I4H4 exhibited ST at input accelerations below 1 G. Therefore, the dual-beam-FCI can generate high output accelerations because ST occurs in a broadband low-frequency region below 20 Hz and under low-acceleration conditions, rendering it highly suitable for the recovery of vibrational energy, which is abundant in the environment.

However, although a slight difference was observed in the required acceleration for ST occurrence in the high-frequency domain across different mass conditions, in the low-frequency domain, a greater integrated mass led to lower input acceleration thresholds for ST occurrence. This is attributed to the decrease in the natural frequency of the second beam as the mass increases, resulting in high second-beam oscillations at lower input frequencies, thereby facilitating ST. Therefore, adjusting the mass of the MEMS VEH and the integrated weights on the second beam of the dual-beam-FCI enables a more efficient recovery of vibrational energy in the low-frequency range below 20 Hz, which exists in various environments.

The input acceleration at which each model integrated a mass of 9.0 g at the center of the second beam induced ST was compared with the theoretically calculated acceleration required for ST. The comparison results are shown in Fig. 9. The horizontal axis represents the frequency of the input acceleration, and the vertical axis represents the acceleration at the occurrence of ST. The experimental and theoretical values are indicated by solid and dashed lines, respectively.

The experimental results show that the acceleration at which ST occurs increases quadratically for all the models. This result aligns with the theoretical values, which are proportional to the square of the frequency, indicating that the ST in the DBMS varies approximately with theoretical predictions. However, in the I4H4 model, although both the experimental and theoretical values exhibit quadratic trends, the difference between them is more pronounced than that in the other geometries. The I4H4 model exhibits ST at lower input accelerations than those predicted analytically. Because the dual-beam-FCI is a two-degree-of-freedom vibrational system comprising a curved first beam and straight second beam, vibrational interactions in which the vibration of the second beam improves or suppresses that of the first beam may occur. Because the analysis in this study is based on the curve of the reaction force obtained via steady-state analysis, it does not account for vibrations specific to a two-degree-of-freedom system. Therefore, we presume that the vibration of the second beam enhances that of the first beam, resulting in lower experimental values than analytical values. In other words, this is likely because the dynamic coupling between the two beams is more pronounced in the I4H4 model, which the present steady-state analytical model does not capture. As a result, the vibration of the second beam can more effectively enhance that of the first beam.

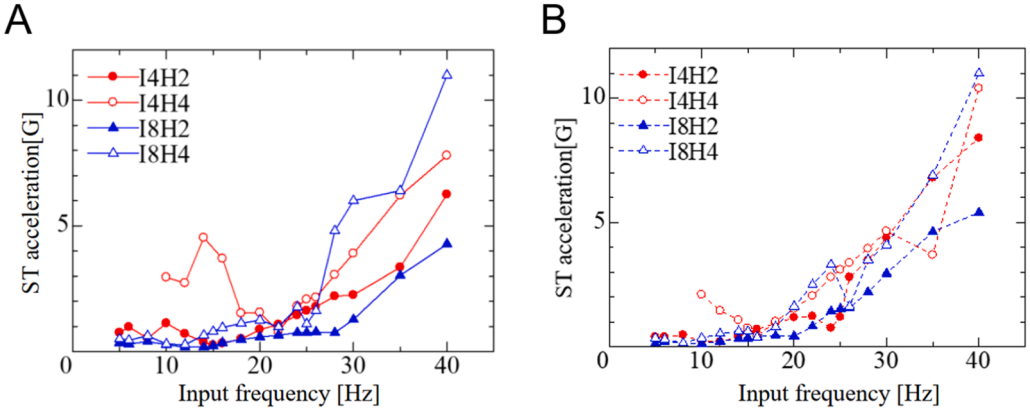


Fig. 8. Input frequency and generated acceleration when ST occurs. (A) Models with masses of 9.0 g on the central part. (B) Models with masses of 18.0 g on the central part.

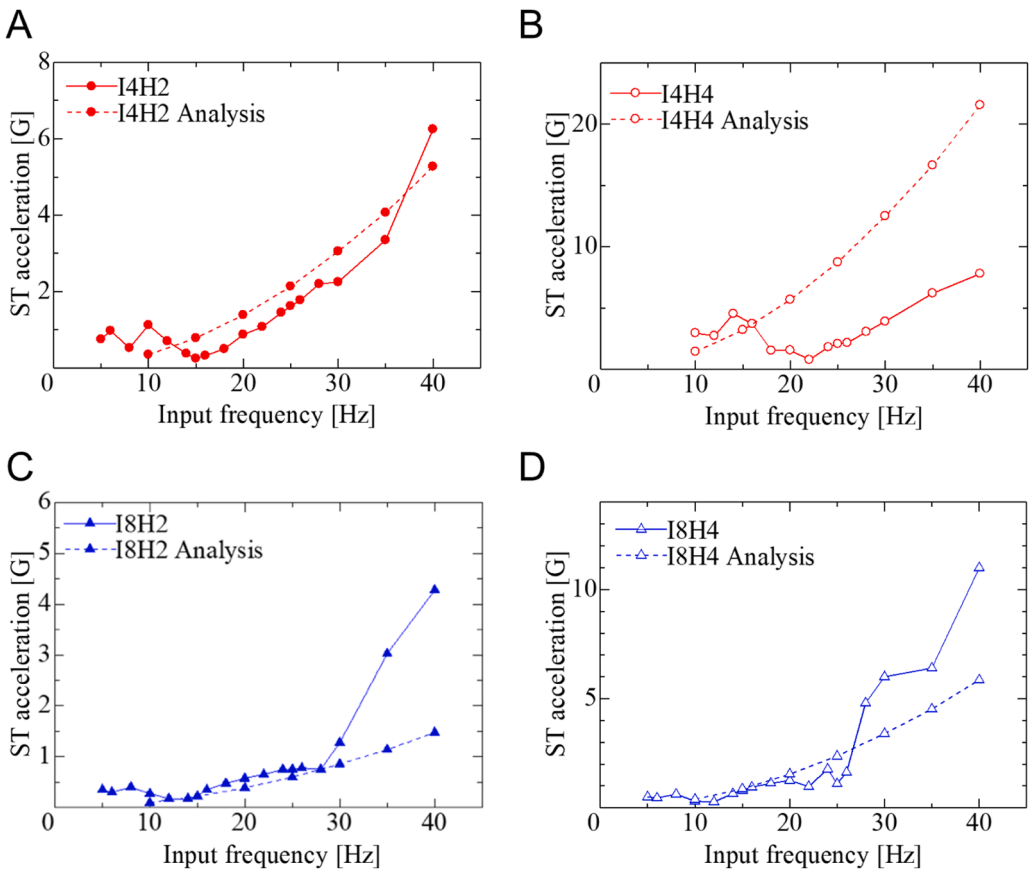


Fig. 9. Frequency of input vibration and analytical and measured accelerations when ST occurs. (A) I4H2 model. (B) I4H4 model. (C) I8H2 model. (D) I8H4 model.

This enhanced coupling reduces the effective threshold for ST, leading to lower experimental values than those predicted analytically.

These results show that the acceleration required to induce ST is determined by the potential barrier inherent to the bistable curved beam and influenced by the frequency of the input acceleration. To induce ST, sufficient input energy must overcome the potential barrier between stable equilibrium positions. However, under periodic vibrations, the magnitude of acceleration required for ST varies with input frequency. Therefore, in two-degree-of-freedom systems such as the DBMS used in this study, designing geometries that match the frequency and acceleration ranges of vibrations present in the operating environment can promote ST-inducing vibrations. This design strategy is expected to broaden the frequency bandwidth for vibrational energy recovery in MEMS VEHs.

5. Considerations for MEMS VEH integration

In this research, a 5-mm-thick PC plate was used as the DBMS material to prevent the bending by gravity due to the high aspect ratio of the structure. Generally, it is difficult to fabricate high-aspect-ratio structure as the microscale compared with the millimeter scale. However, at the microscale, not only do body forces become less significant, but recent advances in microfabrication technologies have also enabled the realization of high-aspect-ratio structures [41]. Therefore, even for microstructures incorporating MEMS VEH, it is reasonable to assume that structural deformation is negligible and does not significantly affect their vibrational behavior.

In a previous study, where acceleration was calculated as the second derivative of the displacement waveform measured using a laser displacement sensor, the output acceleration exceeded the input acceleration by up to 1.3 times only immediately after ST [40]. However, in this study, direct measurement using an acceleration sensor revealed that the output acceleration of the second beam consistently exceeded the input acceleration under all conditions. Moreover, following ST, the output acceleration was consistently more than 2–3 times greater than the input acceleration. This indicates that the acceleration generated by the second beam, which was mechanically coupled to the first beam, was greater than that produced by the first beam only. Consequently, integrating a MEMS VEH onto the second beam enables a more efficient vibrational energy-harvesting strategy compared with the approach in a previous study, where the oscillatory structure of the MEMS VEH was used to trigger the ST of the first beam.

However, in a previous study, the use of a laser displacement sensor to derive acceleration as the second derivative of displacement likely introduced amplified noise in the high-frequency range. By contrast, the direct measurement of output acceleration using an acceleration sensor in this study ensured a more accurate acquisition and evaluation of the output acceleration of the DBMS. Because the electrical output of a MEMS VEH is proportional to the square of the input acceleration, the proposed dual-beam-FCI in this study is expected to theoretically improve power generation by a factor of over 4 [19]. In reality, considering practical constraints such as structural damping, significantly improving the amount of power generation to a theoretically predicted value is challenging. However, the power generation efficiency of MEMS VEHs can be improved without significantly changing the total size of the generation device using the proposed structure, which can be fabricated via semiconductor microfabrication processes. While this study is limited to a millimeter-scale demonstration, future work will focus on evaluating the applicability of the proposed structure to micro- and nano-scale energy harvesting devices.

6. Conclusions

In this study, the vibrational energy transmission capability of a

dual-beam-FCI was evaluated using a DBMS. Modal analysis shows that the dual-beam-FCI can induce an ST without being significantly affected by the mass integrated into the second beam. This indicates that the dual-beam-FCI does not limit the design flexibility of the MEMS VEH. The synthesized oscillatory waveform generated on the second beam exhibited greater acceleration than the input acceleration, and the output acceleration exceeded three times the input acceleration when ST occurred. Because the power generated by the MEMS VEH is proportional to the square of the input acceleration, the use of a dual-beam-FCI is expected to improve the generation efficiency of the MEMS VEH without significantly changing the total size of the generation device. Furthermore, environmental vibrations with frequencies below 20 Hz, which are commonly present in natural settings, can readily induce ST in the first beam with less energy than that calculated theoretically. Therefore, the dual-beam-FCI, which can generate large accelerations via ST without imposing design limitations on the integrated MEMS VEH, is highly suitable for environmental energy harvesting using various MEMS VEHs. As future work, the proposed structure will be scaled down to the micro- or nano-scale using semiconductor manufacturing processes, and its applicability and effectiveness will be evaluated.

CRediT authorship contribution statement

Hidetaka Ueno: Writing – review & editing, Writing – original draft, Validation, Project administration, Methodology, Investigation, Funding acquisition, Conceptualization. **Ryo Ichige:** Writing – original draft, Validation, Methodology, Investigation. **Kota Morishita:** Validation, Investigation. **Hiroshi Toshiyoshi:** Writing – review & editing, Supervision, Project administration, Methodology, Funding acquisition, Conceptualization. **Takaaki Suzuki:** Writing – review & editing, Writing – original draft, Supervision, Project administration, Methodology, Funding acquisition, Conceptualization.

Funding

This research was partially supported by JST CREST (Grant Number JPMJCR19Q2), JSPS KAKENHI (Grant Numbers JP22K14583, JP23K26058, and JP23KK0258), and Gunma University Priority Support Project R07–01.

Declaration of Competing Interest

The authors declare that they have no known competing financial interests or personal relationships that could have appeared to influence the work reported in this paper.

Acknowledgements

We would like to thank Editage (www.editage.jp) for English language editing.

Appendix A. Supporting information

Supplementary data associated with this article can be found in the online version at doi:10.1016/j.sna.2026.118002.

Data availability

Data will be made available on request.

References

[1] Literature Survey on Wireless Sensor Networks, 2014. Int. J. Eng. Res. 3. https://doi.org/10.18535/ijecs/v5i8.202014.
[2] S. Zhang, H. Zhang, A review of wireless sensor networks and its applications, in: 2012 IEEE International Conference on Automation and Logistics. Presented at the 2012 IEEE International Conference on Automation and Logistics (ICAL), IEEE, Zhengzhou, China, 2012, pp. 386–389, https://doi.org/10.1109/ICAL.2012.6308240.
[3] S. Madakam, R. Ramaswamy, S. Tripathi, Internet of Things (IoT): A Literature Review, JCC 03 (2015) 164–173, https://doi.org/10.4236/jcc.2015.35021.
[4] H. Honma, H. Mitsuya, G. Hashiguchi, H. Fujita, H. Toshiyoshi, Improvement of energy conversion effectiveness and maximum output power of electrostatic induction-type MEMS energy harvesters by using symmetric comb-electrode structures, J. Micromech. Micro 28 (2018) 064005, https://doi.org/10.1088/1361-6439/aab514.
[5] J.-Q. Liu, H.-B. Fang, Z.-Y. Xu, X.-H. Mao, X.-C. Shen, D. Chen, H. Liao, B.-C. Cai, A MEMS-based piezoelectric power generator array for vibration energy harvesting, Microelectron. J. 39 (2008) 802–806, https://doi.org/10.1016/j.mejo.2007.12.017.
[6] W.J. Choi, Y. Jeon, J.-H. Jeong, R. Sood, S.G. Kim, Energy harvesting MEMS device based on thin film piezoelectric cantilevers, J. Electroceram 17 (2006) 543–548, https://doi.org/10.1007/s10832-006-6287-3.
[7] M.T. Todaro, F. Guido, V. Mastronardi, D. Desmaele, G. Epifani, L. Algieri, M. De Vittorio, Piezoelectric MEMS vibrational energy harvesters: Advances and outlook, Microelectron. Eng. 183–184 (2017) 23–36, https://doi.org/10.1016/j.mee.2017.10.005.
[8] A.R.M. Siddique, S. Mahmud, B.V. Heyst, A comprehensive review on vibration based micro power generators using electromagnetic and piezoelectric transducer mechanisms, Energy Convers. Manag 106 (2015) 728–747, https://doi.org/10.1016/j.enconman.2015.09.071.
[9] S. Roundy, P.K. Wright, J. Rabaey, A study of low level vibrations as a power source for wireless sensor nodes, Comput. Commun. 26 (2003) 1131–1144, https://doi.org/10.1016/S0140-3664(02)00248-7.
[10] M. Amin Karami, D.J. Inman, Powering pacemakers from heartbeat vibrations using linear and nonlinear energy harvesters, Appl. Phys. Lett. 100 (2012) 042901, https://doi.org/10.1063/1.3679102.
[11] C.R. Saha, T. O'Donnell, N. Wang, P. McCloskey, Electromagnetic generator for harvesting energy from human motion, Sens. Actuator A-Phys. 147 (2008) 248–253, https://doi.org/10.1016/j.sna.2008.03.008.
[12] L. Dhakar, H. Liu, F.E.H. Tay, C. Lee, A new energy harvester design for high power output at low frequencies, Sens. Actuator A-Phys. 199 (2013) 344–352, https://doi.org/10.1016/j.sna.2013.06.009.
[13] H. Liu, C. Lee, T. Kobayashi, C.J. Tay, C. Quan, A new S-shaped MEMS PZT cantilever for energy harvesting from low frequency vibrations below 30 Hz, Microsyst. Technol. 18 (2012) 497–506, https://doi.org/10.1007/s00542-012-1424-1.
[14] R. Ichige, N. Kuriyama, Y. Umino, T. Tsukamoto, T. Suzuki, Size optimization of metamaterial structure for elastic layer of a piezoelectric vibration energy harvester, Sens. Actuator A-Phys. 318 (2021) 112488, https://doi.org/10.1016/j.sna.2020.112488.
[15] H. Liu, C.J. Tay, C. Quan, T. Kobayashi, C. Lee, Piezoelectric MEMS energy harvester for low-frequency vibrations with wideband operation range and steadily increased output power, J. Micro Syst. 20 (2011) 1131–1142, https://doi.org/10.1109/JMEMS.2011.2162488.
[16] T. Tsukamoto, Y. Umino, S. Shiomi, K. Yamada, T. Suzuki, Bimorph piezoelectric vibration energy harvester with flexible 3D meshed-core structure for low frequency vibration, Adv. Mater, Sci. Technol. Adv. Mater. 19 (2018) 660–668, https://doi.org/10.1080/14686996.2018.1508985.
[17] R. K R, A.S. Rao, J. A, R. Pinto, Low frequency piezoelectric P(VDF-TrFE) microcantilevers with a novel MEMS process for vibration sensor and energy harvester applications, Smart Mater. Struct. 28 (2019) 065022, https://doi.org/10.1088/1361-665X/ab19d2.
[18] T. Tsukamoto, Y. Umino, K. Hashikura, S. Shiomi, K. Yamada, T. Suzuki, A Polymer-based Piezoelectric vibration energy harvester with a 3D meshed-core structure, JoVE (2019) 59067, https://doi.org/10.3791/59067.
[19] H. Toshiyoshi, S. Ju, H. Honma, C.-H. Ji, H. Fujita, MEMS vibrational energy harvesters, Adv. Mater, Sci. Technol. Adv. Mater. 20 (2019) 124–143, https://doi.org/10.1080/14686996.2019.1569828.
[20] K. Murotani, Y. Suzuki, MEMS electret energy harvester with embedded bistable electrostatic spring for broadband response, J. Micromech. Micro 28 (2018) 104001, https://doi.org/10.1088/1361-6439/aac8cc.
[21] K. Yamamoto, T. Fujita, A. Badel, F. Formosa, K. Kanda, K. Maenaka, Energy estimation for electret harvester with nonlinear spring. Proceedings of Eurosensors 2017, MDPI, Paris, France, 3&ndash, 2017, pp. 585_1–585_5, https://doi.org/10.3390/proceedings1040585, 6 September 2017.
[22] R.L. Harne, K.W. Wang, A review of the recent research on vibration energy harvesting via bistable systems, Smart Mater. Struct. 22 (2013) 023001, https://doi.org/10.1088/0964-1726/22/2/023001.
[23] S. Palathingal, G.K. Ananthasuresh, Design of bistable arches by determining critical points in the force-displacement characteristic, Mech. Mach. Theory 117 (2017) 175–188, https://doi.org/10.1016/j.mechmachtheory.2017.07.009.
[24] R. Gao, M. Li, Q. Wang, J. Zhao, S. Liu, A novel design method of bistable structures with required snap-through properties, Sens. Actuator A-Phys. 272 (2018) 295–300, https://doi.org/10.1016/j.sna.2017.12.019.
[25] J. Casals-Terre, A. Fargas-Marques, A.M. Shkel, Snap-action bistable micromechanisms actuated by nonlinear resonance, J. Micro Syst. 17 (2008) 1082–1093, https://doi.org/10.1109/JMEMS.2008.2003054.
[26] A. Rafsanjani, A. Akbarzadeh, D. Pasini, Snapping mechanical metamaterials under Tension, Adv. Mater. 27 (2015) 5931–5935, https://doi.org/10.1002/adma.201502809.

[27] B. Andò, S. Baglio, A.R. Bulsara, V. Marletta, A bistable buckled beam based approach for vibrational energy harvesting, Sens. Actuator A-Phys. 211 (2014) 153–161, https://doi.org/10.1016/j.sna.2013.12.027.
[28] L. Tissot-Daguette, H. Schneegans, E. Thalmann, S. Henein, Analytical modeling and experimental validation of rotationally actuated pinned–pinned and fixed–pinned buckled beam bistable mechanisms, Mech. Mach. Theory 174 (2022) 104874, https://doi.org/10.1016/j.mechmachtheory.2022.104874.
[29] A. Cammarano, S.G. Burrow, D.A.W. Barton, Modelling and experimental characterization of an energy harvester with bi-stable compliance characteristics, Proc. Inst. Mech. Eng. Pt. I J. Syst. Contr. Eng. 225 (2011) 475–484, https://doi.org/10.1177/0959651811403093.
[30] S.P. Pellegrini, N. Tolou, M. Schenk, J.L. Herder, Bistable vibration energy harvesters: A review, J. Intell. Mater. Syst. Struct. 24 (2013) 1303–1312, https://doi.org/10.1177/1045389×12444940.
[31] B. Camescasse, A. Fernandes, J. Pouget, Bistable buckled beam and force actuation: Experimental validations, Int. J. Solids Struct. 51 (2014) 1750–1757, https://doi.org/10.1016/j.ijsolstr.2014.01.017.
[32] A. Morel, L. Charleux, Q. Demouron, A. Benhemou, D. Gibus, C. Saint-Martin, A. Carré, É. Roux, T. Huguet, A. Badel, Simple analytical models and analysis of bistable vibration energy harvesters, Smart Mater. Struct. 31 (2022) 105016, https://doi.org/10.1088/1361-665X/ac8d3d.
[33] J. Qiu, J.H. Lang, A.H. Slocum, A Curved-Beam Bistable Mechanism, J. Micro Syst. 13 (2004) 137–146, https://doi.org/10.1109/JMEMS.2004.825308.
[34] J. Qiu, J.H. Lang, A.H. Slocum, A centrally-clamped parallel-beam bistable MEMS mechanism. Technical Digest. MEMS 2001. 14th IEEE International Conference on Micro Electro Mechanical Systems (Cat. No.01CH37090), IEEE, Interlaken, Switzerland, 2001, pp. 353–356, https://doi.org/10.1109/MEMSYS.2001.906551.
[35] S. Park, D. Hah, Pre-shaped buckled-beam actuators: Theory and experiments, Sens. Actuator A-Phys. 148 (2008) 186–192, https://doi.org/10.1016/j.sna.2008.07.009.
[36] D.-A. Wang, H.-T. Pham, Y.-H. Hsieh, Dynamical switching of an electromagnetically driven compliant bistable mechanism, Sens. Actuator A-Phys. 149 (2009) 143–151, https://doi.org/10.1016/j.sna.2008.11.004.
[37] K. Yamamoto, T. Fujita, A. Badel, K. Kanda, K. Maenaka, Design and fabrication of parallel curved spring for nonlinear energy harvester, Procedia Eng. 120 (2015) 651–654, https://doi.org/10.1016/j.proeng.2015.08.697.
[38] K. Yamamoto, T. Fujita, A. Badel, F. Formosa, K. Kanda, K. Maenaka, Vibration energy harvester with bi-stable curved beam spring offset by gravitational acceleration, J. Phys. Conf. Ser. 660 (2015) 012127, https://doi.org/10.1088/1742-6596/660/1/012127.
[39] K. Yamamoto, A. Badel, F. Formosa, L. Charleux, T. Fujita, K. Kanda, K. Maenaka, Non-linear vibration electret-harvester with optimized curved beam for low-frequency operation, J. Phys. Conf. Ser. 1052 (2018) 012122, https://doi.org/10.1088/1742-6596/1052/1/012122.
[40] H. Ueno, H. Toshiyoshi, T. Suzuki, Frequency conversion interposer with no-internal stress curved-beam for MEMS vibrational energy harvesters, Sens. Actuator A-Phys. 378 (2024) 115750, https://doi.org/10.1016/j.sna.2024.115750.
[41] Z. Shi, K. Jefimovs, J. Vila-Comamala, A. Pereira, D. Josell, M. Stampanoni, L. Romano, Deep-reactive-ion-etching in X-ray grating fabrication: a review, Mater. Sci. Semicond. Process. 201 (2026) 110041, https://doi.org/10.1016/j.mssp.2025.110041.

Hidetaka Ueno received his B.E. and M.E. degrees from Kagawa University, Japan, in 2014 and 2016, respectively. He received his Ph.D. degree from Gunma University, Japan, in 2019. From 2019–2020, he was a postdoctoral researcher at Gunma University. From 2020–2023, he was a postdoctoral researcher at the National Institute of Advanced Industrial Science and Technology. Since 2023, he has been a project assistant professor at Kobe University. His research interests include bioengineering. (hueno@people.kobe-u.ac.jp).

Ryo Ichige received his M.E. degree in mechanical engineering from Gunma University, Gunma, Japan, in 2021.

Kota Morishita received his M.E. degree in mechanical engineering from Gunma University, Gunma, Japan, in 2024. He is currently enrolled in the Ph.D. program at Gunma University.

Hiroshi Toshiyoshi received his M.E. and Ph.D. degrees in electrical engineering from The University of Tokyo, Tokyo, Japan, in 1993 and 1996, respectively. He joined the Institute of Industrial Science (IIS), The University of Tokyo, in 1996 as a lecturer. From 1999–2001, he was a visiting assistant professor at the University of California, Los Angeles, CA, U.S.A. In 2002, he became an associate professor with the IIS, The University of Tokyo. From 2005–2008, he was the project leader of the Optomechatronics Project at the Kanagawa Academy of Science and Technology, Kawasaki, Japan. Since 2009, he has been a professor with the IIS, The University of Tokyo. His research interests include optical and power MEMS. (hiro@iis.u-tokyo.ac.jp).

Takaaki Suzuki received his B.E. and M.E. degrees from Gunma University, Japan, in 1998 and 2000, respectively. He also received his Ph.D. degree from Kyoto University, Japan, in 2003. From 2004–2008, he was an assistant professor at Kyoto University. From 2008–2015, he was an associate professor at Kagawa University. From 2015–2018, he was an associate professor at Gunma University. Since 2018, he has been a professor at the Division of Mechanical Science & Technology, Gunma University. From 2015–2019, he was also a PRESTO researcher at the Japan Science and Technology Agency. His research interests include the development of novel microfabrication technology, microfluidic systems for gene and cell analyses, and an energy harvester for IoT. He is a member of IEEE, the Japan Society of Mechanical Engineers, the Institute of Electrical Engineers of Japan, and so forth. (suzuki.taka@gunma-u.ac.jp).